6474 *Chem. Mater.* **2010,** *22,* 6474–6482
DOI:10.1021/cm1026078

CHEMISTRY OF MATERIALS
Article

Photoelectrochemical Performance of Nanostructured Ti- and Sn-Doped α-Fe_2O_3 Photoanodes

Nathan T. Hahn and C. Buddie Mullins*

Departments of Chemical Engineering and Chemistry and Biochemistry, Center for Electrochemistry, Texas Materials Institute, Center for Nano- and Molecular Science, University of Texas at Austin, 1 University Station C0400, Austin, Texas 78712-0231, United States

Received September 10, 2010. Revised Manuscript Received November 4, 2010

Thin films of α-Fe_2O_3 doped with either Ti or Sn were prepared by coevaporating iron and titanium/tin in a reactive oxygen ambient, and their physical, chemical, and photoelectrochemical properties were studied. It was found that manipulating the deposition angle had a profound effect on the photoelectrochemical water oxidation performance of 4% Ti-doped α-Fe_2O_3 films, and a maximum in photocurrent at 1.4 V vs RHE (Reversible Hydrogen Electrode) was achieved for films grown at 75° incidence. It was also found that the nanocolumnar morphology and superior porosity attained using glancing angles improved the relative conversion of visible-light ($\lambda > 420$ nm) photons compared to dense films deposited at normal incidence. Sn-doped films were also prepared for comparison using the same deposition conditions, and although they were substantially better than undoped films, their performance was somewhat below that of Ti-doped films. The Ti-doped films deposited using optimum conditions resulted in incident photon-to-current efficiencies (IPCE) reaching 31% at 360 nm and 1.4 V vs RHE. By comparison, Sn-doped films reached only 21% under the same conditions. The increased photoconversion efficiency brought about through Ti^{4+} or Sn^{4+} incorporation appears to be due to both the improvement of electron transport within the bulk of the film and the suppression of recombination at the film−electrolyte interface due to the stronger electric field near the surface.

Introduction

The search for efficient, robust photocatalytic materials has persisted for nearly 40 years since the ground-breaking work of Fujishima and Honda, which demonstrated the photoelectrochemical oxidation of water over an illuminated semiconducting TiO_2 film.[1] Since this discovery, countless attempts to develop materials capable of producing hydrogen via the "water splitting" reaction have been made with varying degrees of success. The generally quoted suggestion of the necessary solar-to-hydrogen (STH) efficiency requirement for a photoelectrochemical water splitting device stands at 10% in order for the process to attain commercial viability.[2] Of course, along with this conversion efficiency benchmark comes the requirement of long-term stability on the order of several years as well as reasonable affordability. To date, no material or combination of materials has been discovered that can satisfy all of these demands. Most semiconductors having favorable band-gaps and charge transport properties are quite unstable for photoelectrochemistry in aqueous solutions. For instance, Turner et al. demonstrated a monolithic p−n junction water splitting device capable of achieving 12.4% STH efficiency using optimized semiconductors for the individual water oxidation and proton reduction half-reactions but were unable to achieve satisfactory stability.[3]

More recently, research has focused on improving the photoconversion efficiency of inherently stable materials such as metal oxides through nanostructuring or other means, although these materials often either possess too wide a band gap (TiO_2, WO_3) to utilize solar light effectively or poor photoconversion efficiency (α-Fe_2O_3). Incident photon-to-current efficiency (IPCE) values greater than 70% have been attained for photoelectrochemical water oxidation in each of the former cases, although only at relatively short wavelengths ($\lambda < 450$ nm).[4,5] In the latter case, however, lower photoconversion efficiencies are observed for a variety of synthesis techniques.[6−8] For this reason, dopants such as Si,[9,10] Ti,[11,12] Mo,[13]

(1) Fujishima, A.; Honda, K. *Nature* **1972**, *238*, 37–38.
(2) Bard, A. J.; Fox, M. A. *Acc. Chem. Res.* **1995**, *28*, 141–145.
(3) Khaselev, O; Turner, J. A. *Science* **1998**, *280*, 425–427.
(4) Varghese, C. K.; Paulose, M.; Shankar, K.; Mor, G. K.; Grimes, C. A. *J. Nanosci. Nanotechnol.* **2005**, *5*, 1158–1165.
(5) Santato, C.; Ulmann, M.; Augustynski, J. *J. Phys. Chem. B* **2001**, *105*, 936–940.
(6) Khan, S. U. M.; Akikusa, J. *J. Phys. Chem. B* **1999**, *103*, 7184–7189.
(7) Prakasam, H. E.; Varghese, O. K.; Paulose, M.; Mor, G. K.; Grimes, C. A. *Nanotechnology* **2006**, *17*, 4285–4291.
(8) LaTempa, T. J.; Feng, X.; Paulose, M.; Grimes, C. A. *J. Phys. Chem. C* **2009**, *113*, 16293–16298.
(9) Kay, A.; Cesar, I.; Gratzel, M. *J. Am. Chem. Soc.* **2006**, *128*, 15714–15721.
(10) Liang, Y.; Enache, C. S.; van de Krol, R. *Int. J. Photoenergy* **2008**, DOI: 10.1155/2008/739864.
(11) Glasscock, J. A.; Barnes, P. R. F.; Plumb, I. C.; Savvides, N. *J. Phys. Chem. C* **2007**, *111*, 16477–16488.
(12) Sartoretti, C. J.; Alexander, B. D.; Solarska, R.; Rutkowska, W. A.; Augustynski, J.; Cerny, R. *J. Phys. Chem. B* **2005**, *109*, 13685–13692.
(13) Kleiman-Shwarsctein, A.; Hu, Y. S.; Forman, A. J.; Stucky, G. D.; McFarland, E. W. *J. Phys. Chem. C* **2008**, *112*, 15900–15907.

 Published on Web 11/19/2010

Pt,[14] and Al[15] have each been utilized individually to greatly improve the efficiency of α-Fe_2O_3 thin films produced by many different methods, especially in the case of Si-doping through chemical vapor deposition (CVD).[9] In a few cases, combinations of dopants such as Ti/Al and Sn/Be have had a synergistic effect on photoelectrochemical performance.[12,16] Despite these successes, more improvement is clearly necessary if α-Fe_2O_3 is to be utilized as a photocatalyst for water oxidation. The interest in α-Fe_2O_3 stems from its good stability in aqueous environments (pH > 3) and relatively narrow band gap (2.0−2.2 eV).[17] Additionally, although its conduction band edge position is too far positive to produce hydrogen via the reduction of protons, it could be utilized as the photoanode for water oxidation in a tandem photoelectrochemical device.[18]

A number of groups have employed combinatorial techniques to rapidly screen combinations of mixed-metal or doped metal oxides.[16,19−21] One recent study in particular indicated that manipulation of the Ti or Sn concentration in α-Fe_2O_3 is critical to obtaining optimum photocurrent densities, with 4 atom % (M/(M + Fe) = 0.04) giving the best water oxidation performance in both cases.[16] This previous work employed a drop casting method to produce photocatalyst "spots", which are not necessarily uniform and do not possess an optimized morphology for the photoelectrochemical oxidation of water. In the present work, reactive ballistic deposition (RBD) is employed along with glancing angle deposition (GLAD) as a film preparation technique since the codeposition of metal sources in a desired ratio would allow for the preparation of uniform, well controlled, nanostructured thin films having the desired composition. RBD refers to the ballistic physical vapor deposition (PVD) of a material along with the simultaneous reaction of this material with a nondirectional ambient gas,[22,23] and GLAD refers to the ballistic deposition of a material at glancing or oblique angles of incidence (70° or greater).[24−28] The latter technique can be used to prepare nanocolumnar thin films by taking advantage of the self-shadowing growth mechanism arising from the preferential deposition of material on surfaces having direct line-of-sight to the deposition source. At extremely glancing angles, random islands of atoms formed during the initial stages of deposition intercept the majority of the incoming atomic flux, shadowing the regions behind them that no longer have line-of-sight to the source. As deposition continues, these islands evolve into nanocolumnar structures and can be quite porous having extremely high specific surface areas approaching 800−1000 m^2/g.[22,29−31] GLAD has previously been used to deposit films of TiO_2,[32−34] ZnO,[35] and WO_3[36] for solar energy conversion applications. Recently, we demonstrated the preparation and optimization of nanostructured, undoped α-Fe_2O_3 thin films using the RBD technique, and the photoconversion efficiencies of these films compare well with those produced by other methods.[37] For this reason along with the inherent compositional flexibility allowed by coevaporation, it would seem promising to utilize RBD to produce films of α-Fe_2O_3 doped with promising secondary components such as Ti or Sn and investigate their performance for photoelectrochemical water oxidation.

Experimental Section

Film Preparation. Films were deposited onto fluorine-doped tin oxide (FTO) coated glass substrates (Pilkington, TEC15) held at room temperature by evaporating Fe metal along with the desired metal dopant in a background of O_2 under high vacuum conditions ($\sim 10^{-6}$ Torr). The base pressure of the film deposition chamber is approximately 1×10^{-8} Torr, which was increased to approximately 1×10^{-6} Torr by leaking in O_2 (99.99%, Matheson) using a leak valve. Iron and Ti were evaporated from rods (Alfa) having a minimum purity of 99.9% using one home-built and one commercial (Tectra) electron-beam evaporator. Tin was evaporated using tin shot (99.999%, Alfa) heated in a Ta crucible that was mounted in a home-built electron-beam evaporator. Deposition rates were measured prior to depositing the films using a quartz crystal microbalance (QCM, Inficon), which was mounted on a linear translator such that the QCM could be positioned directly where the substrate would be during deposition. The substrate holder could be rotated, allowing for utilization of the entire possible range of deposition angles (0−90°), and the source to substrate distance was approximately 17 cm for all evaporators. A diagram of the deposition scheme is shown in Figure 1. After deposition, the samples were annealed in air at 550 °C for 2 h in a box furnace (Neytech). The temperature was brought from room temperature to the desired annealing

(14) Hu, Y. S.; Kleiman-Shwarsctein, A.; Forman, A. J.; Hazen, D.; Park, J. N.; McFarland, E. W. *Chem. Mater.* **2008**, *20*, 3803–3805.
(15) Kleiman-Shwarsctein, A.; Huda, M. N.; Walsh, A.; Yan, Y.; Stucky, G. D.; Hu, Y.; Al-Jassim, M. M.; McFarland, E. W. *Chem. Mater.* **2010**, *22*, 510–517.
(16) Jang, J. S.; Lee, J.; Ye, H.; Fan, F. R. F.; Bard, A. J. *J. Phys. Chem. C* **2009**, *113*, 6719–6724.
(17) Hardee, K. L.; Bard, A. J. *J. Electrochem. Soc.* **1976**, *123*, 1024.
(18) Miller, E. L.; Rocheleau, R. E.; Khan, S. *Int. J. Hydrogen Energy* **2004**, *29*, 907–914.
(19) Woodhouse, M.; Parkinson, B. A. *Chem. Mater.* **2008**, *20*, 2495–2502.
(20) Arai, T.; Konishi, Y.; Iwasaki, Y.; Sugihara, H.; Sayama, K. *J. Comb. Chem.* **2007**, *9*, 574–581.
(21) Katz, J. J.; Gingrich, T. R.; Santori, E. A.; Lewis, N. S. *Energy Environ. Sci.* **2009**, *2*, 103–112.
(22) Dohnalek, Z.; Kimmel, G. A.; McCready, D. E.; Young, J. S.; Dohnalkova, A.; Smith, R. S.; Kay, B. D. *J. Phys. Chem. B* **2002**, *106*, 3526–3529.
(23) Flaherty, D. W.; Dohnalek, Z.; Dohnalkova, A.; Arey, B. W.; McCready, D. E.; Ponnusamy, N.; Mullins, C. B.; Kay, B. D. *J. Phys. Chem. C* **2007**, *111*, 4765–4773.
(24) Hawkeye, M. M.; Brett, M. J. *J. Vac. Sci. Technol., A* **2007**, *25*, 1317–1335.
(25) Robbie, K.; Brett, M. J. *J. Vac. Sci. Technol., A* **1997**, *15*, 1460–1465.
(26) Robbie, K.; Brett, M. J.; Lakhtakia, A. *Nature* **1996**, *384*, 616.
(27) Abelmann, L.; Lodder, C. *Thin Solid Films* **1997**, *305*, 1–21.
(28) Robbie, K.; Sit, J. C.; Brett, M. J. *J. Vac. Sci. Technol., B* **1998**, *16*, 1115–1122.
(29) Flaherty, D. W.; Hahn, N. T.; Ferrer, D.; Engstrom, T. R.; Tanaka, P. L.; Mullins, C. B. *J. Phys. Chem. C* **2009**, *113*, 12742–12752.
(30) Flaherty, D. W.; May, R. A.; Berglund, S. P.; Stevenson, K. J.; Mullins, C. B. *Chem. Mater.* **2010**, *22*, 319–329.
(31) May, R. A.; Flaherty, D. W.; Mullins, C. B.; Stevenson, K. J. *J. Phys. Chem. Lett.* **2010**, *1*, 1264–1268.
(32) Suzuki, M.; Ito, T.; Taga., Y. *Appl. Phys. Lett.* **2001**, *78*, 3968–3970.
(33) Wolcott, A.; Smith, W. A.; Kuykendall, T. R.; Zhao, Y. P.; Zhang, J. Z. *Small* **2009**, *5*, 104–111.
(34) Kiema, G. K.; Colgan, M. J.; Brett, M. J. *Sol. Energy Mater. Sol. Cells* **2005**, *85*, 321–331.
(35) Wolcott, A.; Smith, W. A.; Kuykendall, T. R.; Zhao, Y. P.; Zhang, J. Z. *Adv. Funct. Mater.* **2009**, *19*, 1849–1856.
(36) Smith, W.; Zhao, Y. P. *Catal. Commun.* **2009**, *10*, 1117–1121.
(37) Hahn, N. T.; Ye, H.; Flaherty, D. W.; Bard, A. J.; Mullins, C. B. *ACS Nano* **2010**, *4*, 1977–1986.

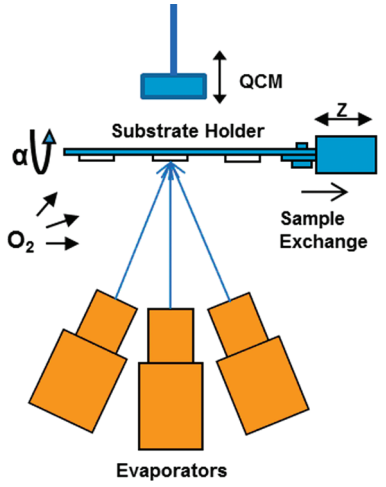

Figure 1. Diagram of the deposition chamber indicating the orientation of the evaporators and substrate holder.

temperature at a rate of 10 °C/min, and the samples were allowed to cool naturally after the desired hold time was reached.

Film Characterization. Scanning electron microscopy (SEM) was performed on a LEO 1530 SEM using a 10 kV focus voltage and on a Hitachi S-5500 scanning transmission electron microscope (STEM) using a 30 kV focus voltage. The Hitachi S-5500 was also used to perform energy dispersive X-ray spectroscopy (EDS) for elemental analysis. Porosity (P) was calculated using the following equation:

$$P = \frac{D_p - D_d}{D_p} \times 100\% \quad (1)$$

Here, D_p is the thickness of the porous film and D_d is the thickness of a dense film consisting of the same amount of deposited material. Standard X-ray diffraction (XRD) and grazing incidence X-ray diffraction (GIXRD) experiments utilized a Bruker D8 diffractometer. UV−vis transmission spectra were taken with a Cary 5000 spectrophotometer using a blank substrate as a baseline standard. Optical penetration depths (α^{-1}) were calculated using the Beer−Lambert law:

$$\alpha^{-1} = -\frac{D}{\ln T} \quad (2)$$

Here, α is the absorption coefficient, D is the thickness of the film, and T is the measured transmittance. Therefore, α^{-1} is the distance over which photons of the wavelength of interest are attenuated to an intensity equal to their original intensity multiplied by 1/e (0.368). X-ray photoelectron spectroscopy (XPS) was performed using a Kratos AXIS X-ray photoelectron spectrometer. A Veeco surface profiler was used to measure the thickness of dense films and quantify sputtering rates for XPS depth profiles.

Electrochemical Testing. The electrochemical and photoelectrochemical properties of each sample were tested using a 3-electrode electrochemical cell with a Ag/AgCl reference electrode and Pt wire counter electrode. The working electrode (the photoanode consisting of the α-Fe_2O_3 film) with illuminated area 0.21 cm^2 was immersed in 1 M KOH and illuminated using a 100 W xenon lamp (Newport) through a UV/IR filter (Schott, KG3). A monochromator (Newport) was also employed to study spectral response and was used in conjunction with a power meter and photodiode (Newport) to calculate the IPCE, given by

$$\text{IPCE} = \frac{1240 \times j_{ph}}{\lambda \times I} \times 100\% \quad (3)$$

Here, j_{ph} is the steady-state photocurrent density, λ is the wavelength of the incident light, and I is the light power intensity at the film surface. A potentiostat (CH Instruments, CHI832) was operated by a desktop computer to perform electrochemical measurements. Electrochemical impedance spectroscopy (EIS) was performed using a CHI 660 electrochemical workstation. Plots of inverse square capacitance (C^{-2}) versus potential (E) can be used to determine the flat-band potential (E_{fb}) and donor density (N_d) of n-type semiconductor films using the Mott−Schottky equation:

$$\frac{1}{C^2} = \frac{2}{e\varepsilon\varepsilon_0 N_d} \times \left(E - E_{fb} - \frac{kT}{e}\right) \quad (4)$$

Here, e is the elementary charge, ε is the dielectric constant of the electrode material, ε_o is the permittivity of vacuum, and C is the capacitance of the electrode. The x-intercept of a linear fit to a plot of C^{-2} versus E reveals the flat-band potential while the slope of this fit can be used to calculate N_d.

Results and Discussion

Preliminary Characterization. XRD profiles for 0% and 4% Ti doped films roughly 360 nm thick are shown in Figure 2a. Only a slight increase in the relative peak intensities of the hematite (PDF# 97-002-4004) (110) and (113) planes could be observed in the doped film. An enhancement in the (110) orientation of the film could provide for improved electron transport vertically through the film due to the higher conductivity of this plane relative to others in hematite, although this may be a minor effect.[9,11] UV−vis spectra for 180 nm thick films deposited at 75° with 0 and 4% Ti are shown in Figure 2b. Both spectra show features typical of α-Fe_2O_3 films with an absorption onset of about 575 nm (2.2 eV), shoulder at 540 nm (2.3 eV), and peak at 430 nm (2.9 eV), which are due to the well-known indirect Fe^{3+} 3d−3d and direct O^{2-} 2p−Fe^{3+} 3d transitions.[38] No obvious changes in the optical absorption of α-Fe_2O_3 caused by Ti incorporation could be observed at these concentrations. Different background O_2 pressures were also employed during the deposition of Ti-doped films at 75° to see if any differences in film crystallography arose. The ratio of O_2 to Fe atomic flux was varied between 0:1 and 20:1, and all samples were subjected to the standard 2 h, 550 °C heat treatment in air. The GIXRD results for these samples showed no evidence for other iron oxide phases besides hematite, and there was little to no discernible trend in the preferred orientation of the films with all showing (104) as the dominant diffraction peak (Figure S1, Supporting Information).

Electron Microscopy. To study the effect of morphology on the performance of Ti-doped α-Fe_2O_3 films, various deposition angles ranging from 0° to 80° were used, employing a Fe/Ti deposition ratio of 24:1 (4% Ti) as determined by QCM calibration before each growth. This composition was selected on the basis of the previously mentioned combinatorial screening results.[16] Two to three films were deposited at each angle. All film thicknesses were maintained at about 180 nm, and the porosity of the films could, thus, be determined by calculating the total number of iron and titanium atoms deposited using

(38) Anderman, M.; Kennedy, J. H. In *Semiconductor Electrodes*; Finklea, H. O., Ed.; Elsevier: Amsterdam, 1988; Chapter 3.

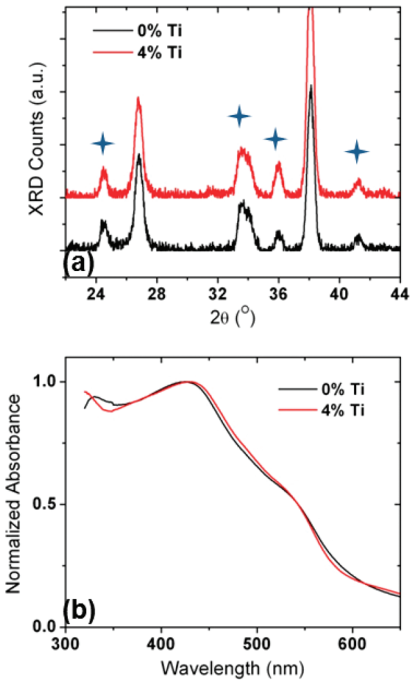

Figure 2. (a) XRD profiles for films deposited at 75° incidence having thicknesses of approximately 360 nm and annealed to 550 °C for 2 h both with and without 4% Ti incorporation. Expected peak locations for hematite (PDF #97-002-4004) are indicated by stars. (b) UV−vis absorbance spectra for films deposited at 75° incidence, also with and without 4% Ti incorporation.

the QCM calibration and comparing this to the number of metal atoms required to deposit a dense film at normal incidence of the same thickness (see eq 1). The porosities of the films deposited at 55°, 70°, 75°, and 80° are estimated (employing eq 1) to be approximately 12%, 35%, 47%, and 60%, respectively, after annealing to 550 °C. These values roughly agree with expected trends in porosity evolution in films prepared by GLAD, as calculated from geometric considerations.[39] SEM images of representative samples are shown in Figure 3. The appearances of the doped films are quite similar to those of undoped α-Fe_2O_3 deposited at the same angles, indicating that this level of Ti incorporation had little to no effect on their morphology.[37] High-resolution SEM images of sections of a 360 nm film deposited at 75° incidence and scraped off onto a lacey carbon grid are shown in Figure 4 in order to provide a clearer view of the film morphology. The individual hematite crystal grains are clearly visible at this level of resolution. The effect of the high annealing temperatures on nanoscale morphology is somewhat noticeable when the SEM image of a Ti-doped film deposited at 75° and annealed at 400 °C (the lowest temperature at which these α-Fe_2O_3 films could be crystallized) is compared to one annealed at 550 °C (Figure S2, Supporting Information). This reduction of nanoscale features and corresponding loss of surface area theoretically decrease photoconversion efficiency, but the poorer performance of films annealed to temperatures less than 550 °C indicates that superior crystallinity and/or a reduced number

(39) Poxson, D. J.; Mont, F. W.; Schubert, M. F.; Kim, J. K.; Schubert, E. F. *Appl. Phys. Lett.* **2008**, *93*, 101914.

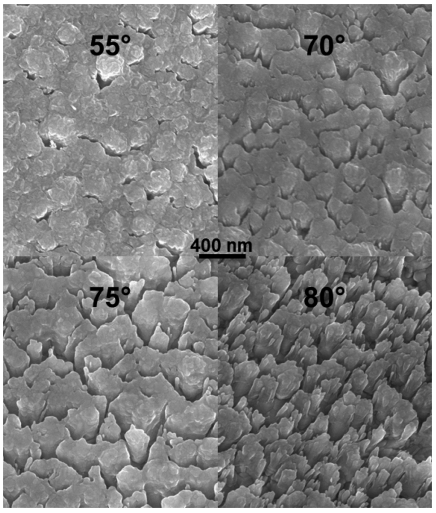

Figure 3. SEM images of 4% Ti-doped films approximately 180 nm thick and deposited at various angles.

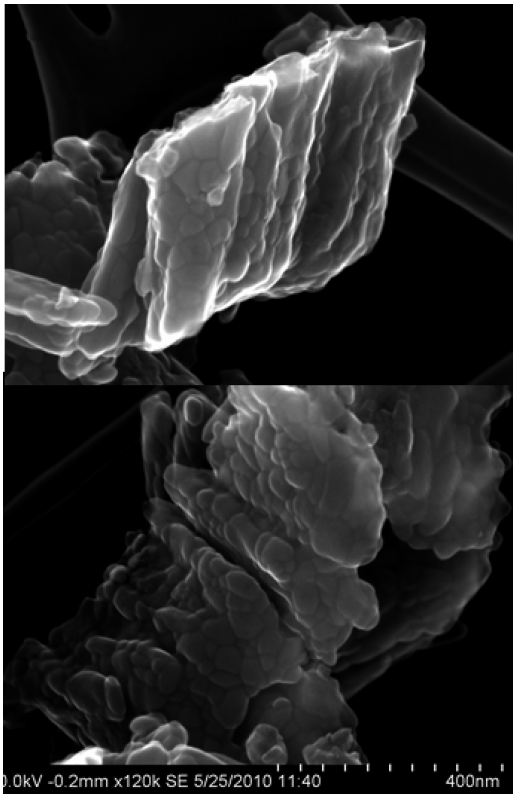

Figure 4. HRSEM images of sections of 4% Ti-doped films deposited at 75° incidence.

of surface defects overcome this drawback at higher temperatures.

Water Oxidation Performance. The water oxidation performance in 1 M KOH for films deposited at various angles from 0° to 80° and annealed to 550 °C is shown in Figure 5. Films deposited at 75° incidence showing significantly higher photocurrents at 0.4 V vs Ag/AgCl (1.4 V vs RHE (Reversible Hydrogen Electrode)) than those deposited at other angles. These films show over 50% greater white light photocurrent than films deposited at 0° incidence (585 vs 375 $\mu A/cm^2$). At this potential, the

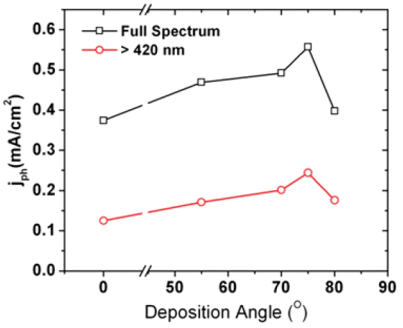

Figure 5. Photocurrent at 1.4 V vs RHE for 4% Ti-doped films deposited at various angles.

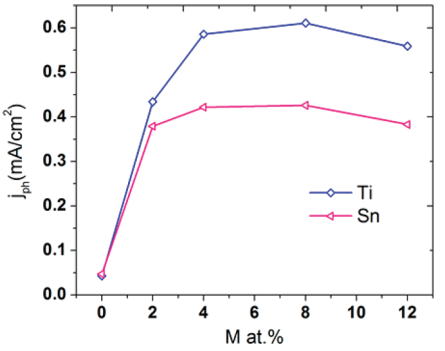

Figure 6. Photocurrent at 1.4 V vs RHE for different doping levels of Ti or Sn.

band-bending within the film should be quite strong, allowing the bulk solid-state processes within the film to dominate the photocurrent response, rather than charge transfer limitations at the surface.[38] The strong photocurrent response of Ti-doped films deposited at very glancing angles (75° and 80°) is quite different from what was observed for undoped α-Fe_2O_3 films, which only performed well when deposited at angles ≤70°.[37] This may be a result of the suppression of recombination at the surface, which is a greater problem at more glancing angles, possibly due to a larger number of surface defects as discussed in more detail below.

Typically, the photocurrent enhancement by the substitution of Ti^{4+} for Fe^{3+} is thought to arise from the improvement of electron transport in bulk α-Fe_2O_3,[9] which is carried out by a polaron hopping mechanism in which electrons hop from Fe^{2+} to Fe^{3+} sites via thermal activation rather than by free conduction, hence the poor measurable electron mobility reported in the literature.[38] It has been observed that the charge compensation of incorporated Ti^{4+} (or M^{4+} in general) via the reduction of additional Fe^{3+} species to Fe^{2+} increases the n-type conductivity of α-Fe_2O_3 single crystals and films.[38] Another effect of increasing the donor density by Ti^{4+} incorporation is a reduction of the depletion layer width, which should increase the strength of the electric field within the semiconductor near the film−electrolyte interface and improve the separation of photogenerated charge carriers in this region. The passivation of recombination at grain boundaries has also been suggested as a possible reason for the improved photoconversion efficiency of Ti- or Si-doped α-Fe_2O_3 films.[11]

Films of 4% Ti-doped Fe_2O_3 that were deposited at 75° with a thickness of 360 nm showed almost identical performance to the 180 nm films, whereas films of undoped α-Fe_2O_3 produced by RBD showed diminishing activity as their thickness was increased beyond 180 nm.[37] This reveals that vertical electron transport through the film is improved by Ti-doping. Cesar et al. showed that Si-doped α-Fe_2O_3 electrodes produced by CVD did not suffer from a decreased in photocurrent for films as thick as 700 nm, which was also quite different from the behavior of their undoped α-Fe_2O_3 films.[40] The addition of a +4 dopant in these cases appears to improve electron transport from the top of the film to the conductive substrate.

In order to test another +4 dopant, Sn was evaporated along with Fe using a Sn/Fe ratio of 1:24. The incorporation of Sn^{4+} was confirmed by XPS (Figure S3, Supporting Information). These films were deposited at 75° incidence and had thicknesses of ~180 nm. There was a clear increase in the performance of the Sn-doped films relative to undoped films prepared using the same conditions, although they still fell short of the Ti-doped films. Films with even higher Sn concentrations (up to 12%) were prepared, but 4−8% appeared to be the optimum range for both Sn and Ti (Figure 6).

The differences in performance between the Ti- and Sn-doped electrodes might be related to the size of the dopant ion. A recent study on Al^{3+} doped Fe_2O_3 used density functional theory (DFT) calculations to indicate that a contraction of the hematite lattice could enhance its polaronic conductivity to some extent by improving the rate of carrier hopping between cations.[15] However, in this work, that behavior was only explicitly predicted for iso-valent doping in α-Fe_2O_3 (substituting a foreign +3 species for Fe^{3+}). The ionic radii of Ti^{4+} and Sn^{4+} are 61 and 69 pm, respectively (Fe^{3+} is 65 pm). It may be reasonable to expect that, as long as the hematite crystal structure is maintained, substituting a smaller +4 species such as Ti^{4+} for Fe^{3+} could induce similar changes in unit cell volume, enhancing polaronic conductivity and, assuming conduction remains dominated by polarons, the photocurrent. Conversely, substituting the larger Sn^{4+} ion for Fe^{3+} would not have this benefit, which lessens its positive impact on photoelectrochemical performance compared to Ti-doping. Berry et.al. found that doping α-Fe_2O_3 with Sn or Ti did in fact alter the unit cell volume in the manner expected (slight increase for Sn and slight decrease for Ti) when 10% of the dopant was incorporated via the hydrothermal method.[41] In the present work, XRD measurements of 12% Ti films seem to reveal a slight contraction of the (110) *d*-spacing relative to 12% Sn films as indicated by a slight increase in the 2θ value for the (110) diffraction peak (Figure S4, Supporting Information). However, these films showed somewhat worse performance than

(40) Cesar, I.; Sivula, K.; Kay, A.; Zboril, R.; Graetzel, M. *J. Phys. Chem. C* **2009**, *113*, 772–782.

(41) Berry, F. J.; Greaves, C.; Helgason, O.; McManus, J.; Palmer, H. M.; Williams, R. T. *J. Solid State Chem.* **2000**, *151*, 157–162.

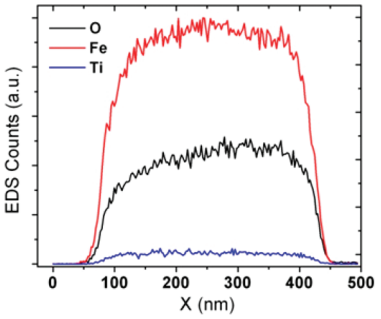

Figure 7. Vertical EDS line scan of a section of 4% Ti-doped film deposited at 75° incidence.

those doped with only 4% Ti or Sn, and the much more prominent (104) peak of 12% Ti doped α-Fe_2O_3 films may indicate that superior overall crystallinity is the more critical factor. Interestingly, the best performing α-Fe_2O_3 films to date are doped with Si^{4+},[9] which has an ionic radius of only 40 nm, far smaller than any transition metal +4 species, indicating that the size of the dopant atom may indeed have an effect on the photoelectrochemical performance. However, another reason for the photocurrent enhancement by reducing dopant size could be an improved ability to incorporate at interstitial sites or to diffuse to and passivate grain boundary states.

Chemical Characterization. The incorporation and distribution of Ti atoms was characterized using EDS and XPS techniques. To perform EDS, a 360 nm thick film deposited at 75° incidence was scraped off of the FTO substrate and deposited on a TEM grid so that the distribution of Ti could be observed. EDS line scans indicate that the distribution of Ti is fairly uniform within the nanocolumnar structures (Figure 7) with no obvious signs of segregation. This is quite different from the behavior observed for dense films, in which Ti was segregated quite far from the surface during annealing (Figure S5, Supporting Information). XPS performed on a film deposited at 75° incidence having 4% Ti and annealed to 550 °C reveals that Ti is in the +4 state as evidenced by the $2p_{1/2}$ and $2p_{3/2}$ peaks present in the Ti 2p spectrum at 458.5 and 464 eV, respectively (Figure 8). The Fe 2p spectrum, also shown in Figure 6, possesses the typical $2p_{1/2}$ and $2p_{3/2}$ peaks of Fe^{3+}. The calculated concentration of Ti (on a metals basis) from the XPS spectra of O, Ti, and Fe is 3.5%. Although some evidence for the reduction of Fe^{3+} to Fe^{2+} would be expected from the substitution of 3.5% Ti^{4+} for Fe^{3+}, no Fe^{2+} satellite peaks at 715 or 730 eV could be observed. This may be because the overall atomic concentration of Ti is quite low (1.33%), and only a small amount of the Ti^{4+} ions are compensated by the formation of Fe^{2+} ions. On the other hand, any Fe^{2+} species present may simply not remain in this state at the surface due to the oxidizing annealing conditions employed here.

A number of groups have investigated the doping of Ti into α-Fe_2O_3 from both theoretical and experimental perspectives to attempt to explain how Ti is incorporated and how this incorporation affects the electronic structure of the parent hematite material. The hematite lattice consists of a hexagonally close-packed array of O^{2-} ions with Fe^{3+}

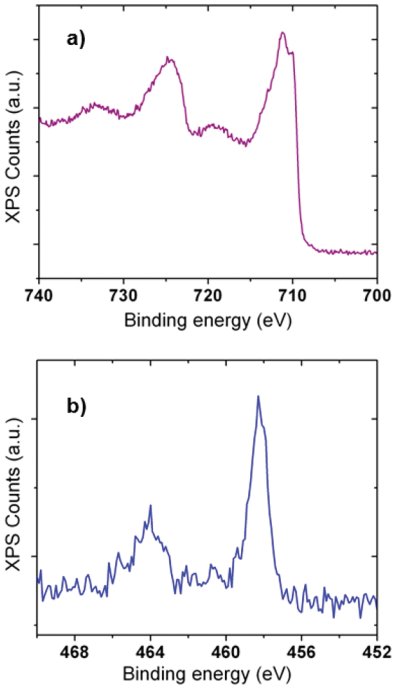

Figure 8. XPS 2p spectra of a 4% Ti-doped film deposited at 75° incidence for (a) Fe and (b) Ti.

ions occupying 2/3 of the associated octahedral sites, and in general, Ti^{4+} (or other cationic dopant) ions may substitute for Fe^{3+} ions at these octahedral sites and/or occupy interstitial octahedral sites. Authors have suggested that the most energetically favorable process is one in which groups of three Ti^{4+} ions are incorporated as "defect clusters" at both substitutional and interstitial octahedral sites with the removal of four Fe^{3+} ions as the charge compensating mechanism.[42] Others have calculated that in the substitutional case the extra electron from Ti^{4+} is likely to be localized on an adjacent Fe^{3+} species, reducing it to Fe^{2+} and giving the typically observed increase in n-type conductivity upon M^{4+} substitution.[43] The former observation is based on a relatively large dopant concentration (M/(M + Fe) = 0.2) whereas the latter considers M/(M + Fe) = 0.04, which could account for the difference in their conclusions. In the present work, no reduction to Fe^{2+} is observed using XPS, but this could be due to differences at the surface and may not be indicative of the bulk state of Fe.

Mott−Schottky Analysis. Electrochemical impedance spectroscopy (EIS) was employed to study the electronic properties of both Ti-doped and undoped films deposited at 75° incidence. The films were analyzed in the dark at pH 13.5. In order to minimize the effect of exposing bare FTO to the electrolyte, a thin (~6 nm), dense layer of Ti-doped iron oxide was deposited on the substrate at normal incidence before depositing the nanocolumnar films. Representative Mott−Schottky plots for films containing 0% and 4% Ti are shown in Figure 9. A minor

(42) Berry, F. J.; Bohorquez, A.; Moore, E. A. *Solid State Commun.* **1999**, *109*, 207–211.
(43) Velev, J.; Bandyopadhyay, A.; Butler, W. H.; Sarker, S. *Phys. Rev. B* **2005**, *71*, 205208.

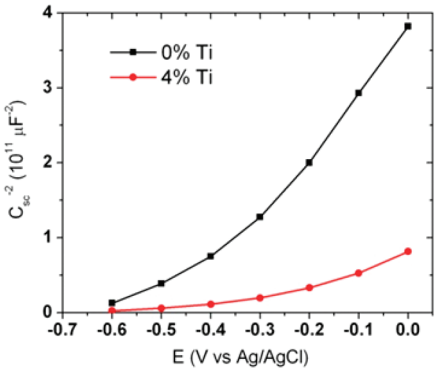

Figure 9. Mott−Schottky plots for films deposited at 75° incidence on top of a dense blocking layer deposited at 0° incidence.

dependence on AC frequency was observed, and the plots displayed in Figure 5 were recorded at 1000 Hz. Films both with and without Ti showed super linear behavior similar to what was observed for Si-doped α-Fe_2O_3 films by others, which was attributed to a decrease in the active surface area of nanostructured films as a function of potential.[40] The theory is that as nanoscale features on the surface become fully depleted they no longer contribute to the effective capacitive surface area, resulting in a changing capacitance with potential. The slope in the quasi-linear regions of the Mott−Schottky plots near E_{fb} (between −0.4 and −0.55 V vs Ag/AgCl) where the depletion layer remains very thin and results in a nearer approximation to a flat electrode was used to calculate donor densities of 2.0×10^{19} and 1.2×10^{20} cm^{-3} for the undoped and 4% Ti-doped films, respectively. The value calculated for the undoped film deposited at 75° incidence is much higher than that calculated in a previous work for a film deposited at normal incidence (1×10^{17} cm^{-3}).[37] Clearly, the nanostructured morphology affects the calculated donor density. The apparent donor density of the Ti-doped film is approximately 9×10^{19} cm^{-3} greater than that of the undoped film, and if an Fe^{3+} density of 4×10^{22} cm^{-3} is assumed for hematite, this represents a donor incorporation of only 0.23%, much lower than the bulk incorporation level of Ti measured by XPS and EDS. This could mean that only a small fraction of Ti^{4+} incorporation results in the reduction of Fe^{3+} to Fe^{2+} and that the rest is compensated via the defect clusters involving Fe^{3+} vacancies suggested by Berry et.al.[42] Flat band potentials (E_{fb}) of −0.61 V vs Ag/AgCl (0.41 V vs RHE) and −0.62 vs Ag/AgCl (0.38 V vs RHE) were calculated for the undoped and 4% Ti-doped electrodes, respectively, showing that E_{fb} was not significantly affected by Ti incorporation.

The increased donor density as a result of Ti-doping decreases the space−charge layer thickness and, consequently, strengthens the electric field near the film−electrolyte interface for a given applied potential, which should lead to more effective separation and transport of electrons and holes in the outer regions of the film and may be a significant reason for the improvement in photocurrent response. However, doping with Sn^{4+} increased the donor density by a similar amount yet did not improve the photocurrent response to the same degree, meaning other characteristics of Ti cause it to be a superior dopant in RBD grown α-Fe_2O_3 films.

Deposition Angle Effects. Several different photoelectrochemical tests were performed to elucidate the effects of deposition angle on the photocurrent response of the 4% Ti-doped α-Fe_2O_3 electrodes. Light chopping experiments were performed between 0.6 and 1.6 V vs RHE to study transient photocurrent response. For all films, the ratio of transient to steady-state photocurrent decreased with increasing applied potential, which is a well-documented behavior on semiconductor electrodes and on α-Fe_2O_3 in particular.[38] The generally accepted theory is that when a photoanode is illuminated there is an initial buildup of intermediate oxidation products on the electrode surface, and as their concentration increases during this initial period, they begin to scavenge photoelectrons generated and/or trapped at this surface resulting in a cathodic current that acts to decrease the observed anodic current until a steady state is achieved.[38] Once illumination is halted, this cathodic current persists until the intermediates are exhausted, resulting in cathodic current spikes when the light is blocked. The extent of these recombination events is probably related to the number of electron trap sites on the electrode surface since electrons located in these traps are unable to migrate away from the surface under low band-bending conditions (at lower applied potentials) and are left to react with a surface electron scavenger.[44] Under high band-bending conditions, more of these electrons are able to escape these surface states via the stronger electric field and, thus, avoid being scavenged. The ratio of transient to steady-state photocurrent at a given potential, then, may reveal whether the surface trapping of electrons and subsequent back reaction are significant limiting factors for the water oxidation performance of a given film.

In this work, a positive trend in the transient to steady-state photocurrent ratio was observed as deposition angle was increased, indicating that films deposited at more glancing angles possess a greater number of surface defects and traps, thus limiting the steady-state photocurrent, most notably at lower potentials. As an example, $j-E$ curves under chopped illumination for films deposited at 0° and 80° incidence are shown in Figure 10. However, although surface recombination appears to be a more significant problem in the films deposited at glancing angles, their morphologies appear to facilitate better bulk charge separation and transport as evidenced by the higher transient photocurrents (that is, before back reaction becomes a significant problem). Interestingly, films deposited at 75° but without Ti incorporation exhibit very large transient to steady-state photocurrent ratios even compared to the Ti-doped films deposited at 80°, which may indicate that the stronger band-bending near the surface of the film as a result of doping drives electrons away from surface traps more readily, and they are less likely to react with surface species. This effect was also observed for Sn-doped films.

(44) Rao, M. V.; Rajeshwar, K.; Pal Verneker, V. R.; DuBow, J. *J. Phys. Chem.* **1980**, *84*, 1987–1991.

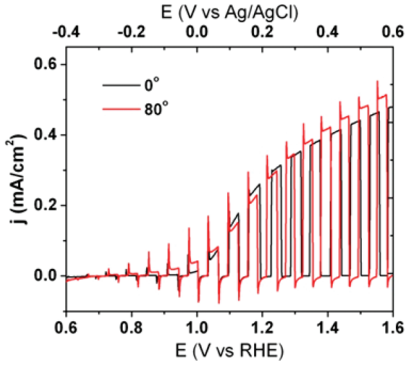

Figure 10. Chopped light experiments using full spectrum illumination for 4% Ti-doped films deposited at 0° and 80° incidence.

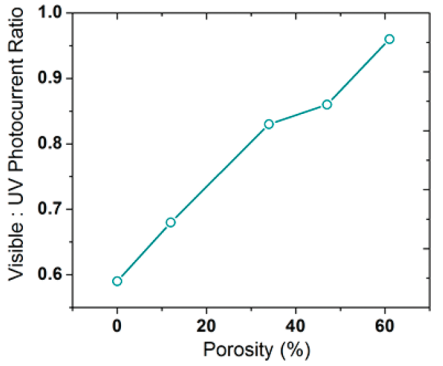

Figure 11. Ratio of visible-light to UV-light contributions to the photocurrent at 1.4 V vs RHE as a function of the calculated porosity of 4% Ti-doped films deposited at angles ranging from 0° to 80°.

Deposition angle was also observed to affect the relative contributions of visible and UV photons to the photocurrent. Due to its indirect band gap, an α-Fe_2O_3 film does not absorb visible photons ($\lambda > 420$ nm) with a high probability, resulting in significantly longer α^{-1} as the wavelength of incident photons is increased. For example, the α^{-1} of a 470 nm photon is twice that of a 370 nm photon in α-Fe_2O_3 (50 vs 25 nm), as measured for a dense film. A highly porous or nanocolumnar film allows more of these more deeply penetrating visible photons to be absorbed relatively close the electrolyte interface since this interface permeates through much of the film, decreasing the required transport distance of the resulting photoholes and reducing their probability of recombining with electrons in the bulk. The ratio of visible to UV photocurrent was observed to increase with increasing deposition angle. In fact, when plotted against the estimated porosity of the films, it shows an almost linear dependence over this range of porosities (Figure 11). This seems to indicate that the nanostructuring brought about by utilizing more glancing angles improves the relative conversion of photons absorbed more deeply within the film, which helps to increase the visible-light conversion efficiency of Ti-doped α-Fe_2O_3.

Photoconversion Efficiency. IPCE tests were performed in 1 M KOH to evaluate the spectral response for water oxidation between 340 and 600 nm of the Ti-doped and Sn-doped α-Fe_2O_3 deposited at 75° (Figure 12). Using a potential of 1.4 V vs RHE, the Ti-doped film reached IPCE values of 31% and 17% at 360 and 420 nm. Unfortunately, these values dropped significantly at longer wavelengths (i.e., < 4% at 500 nm), indicating that the conversion of photons in the green to yellow region of the visible spectrum is still quite poor. The Sn-doped film reached IPCE values of 21% and 11% at the same wavelengths. When the IPCE values are integrated over the AM1.5 solar spectrum,[45] they result in solar photocurrents of 0.94 and 0.63 mA/cm^2, respectively, which, although superior to previously reported films of Ti-doped α-Fe_2O_3 (0.57 mA/cm^2),[11] still fall well short of Si-doped photoanodes showing greater than 2.0 mA/cm^2.[40] Both

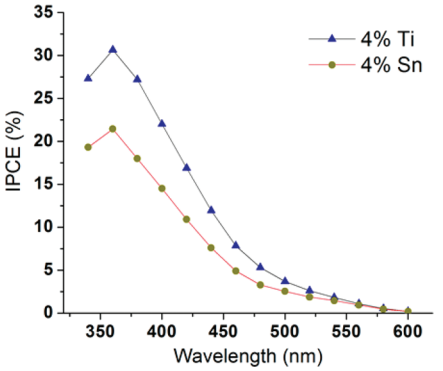

Figure 12. IPCE performance at 1.4 V vs RHE for films deposited at 75° incidence with either 4% Ti or 4% Sn.

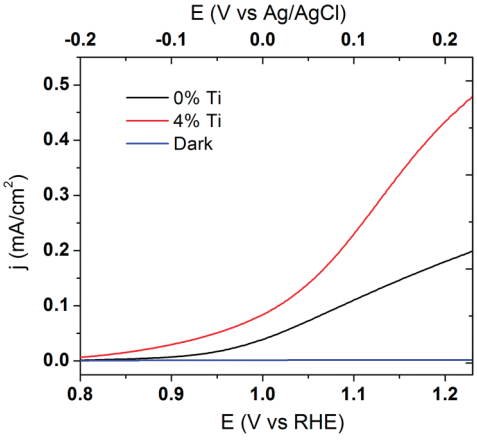

Figure 13. Photoelectrochemical $j-E$ curves comparing the performance of an optimized 4% Ti doped film (75° incidence, 550 °C anneal) to an optimized undoped film (55° incidence, 450 °C anneal) at lower applied potentials under full spectrum illumination.

films performed much better than the best undoped films studied in our previous work on α-Fe_2O_3 prepared by RBD, which reached only 16% at 350 nm using a slightly more positive applied potential of 1.5 V vs RHE.[37] Since in a realistic photoelectrochemical system lower applied potentials would be employed, it was important to note that this improvement in performance due to doping was not solely evident at very positive potentials (> 1.23 V vs RHE). In fact, optimized Ti-doped films outperform optimized

(45) NREL AM 1.5 Gobal solar spectrum derived from SMARTS v.2.9.2; http://rredc.nrel.gov/solar/spectra/am1.5/.

undoped films over the entire range of potentials tested by a factor of 2 or more (Figure 13).

Conclusions

Reactive ballistic deposition (RBD) was employed along with glancing angle deposition (GLAD) to deposit nanostructured films of M-doped α-Fe_2O_3 by evaporating Fe and Ti or Sn simultaneously in vacuum by e-beam bombardment. Titanium doping resulted in a higher photocurrent when each were incorporated at a level of approximately 4 atom %. Incorporating M^{4+} into α-Fe_2O_3 appears to improve charge transport while decreasing recombination both in the bulk and on the surface of the film. The effects of doping with Ti were investigated further while manipulating the morphology and porosity of the films by varying the deposition angle. A clear effect of the deposition angle on the photocurrent at 1.4 V vs RHE could be observed with a deposition angle of 75° giving the highest value under Xe lamp illumination. Additionally, porous films deposited at glancing angles showed a greater contribution of visible light ($\lambda > 420$ nm) photons to the photocurrent. IPCE results for the optimized films show good conversion of UV photons at 1.4 V vs RHE, with quantum yields exceeding 30% at 360 nm, but the visible light conversion efficiency, although somewhat improved by nanostructuring, remains poor, limiting the films' AM1.5 photocurrent significantly.

Acknowledgment. The authors gratefully acknowledge (i) the Division of Chemical Sciences, Geosciences, and Biosciences, Office of Basic Energy Sciences of the U.S. Department of Energy through Grant DE-SC0002219 for funding this work, (ii) a Grant (No. 0618242) from the National Science Foundation for funding the X-ray Photoelectron Spectrometer used for these studies, and (iii) the Welch Foundation (Grant F-1436).

Supporting Information Available: XRD, XPS, and SEM data, as noted in the text (PDF). This material is available free of charge via the Internet at http://pubs.acs.org.